

Theoretical proposal of a revolutionary water-splitting photocatalyst: The monolayer of boron phosphide

Tatsuo Suzuki (✉ dr.tatsuosuzuki@gmail.com)

Tokyo Metropolitan College of Industrial Technology <https://orcid.org/0000-0001-6659-7717>

Article

Keywords:

Posted Date: March 31st, 2022

DOI: <https://doi.org/10.21203/rs.3.rs-1505639/v1>

License:  This work is licensed under a Creative Commons Attribution 4.0 International License.

[Read Full License](#)

Version of Record: A version of this preprint was published at Applied Surface Science on October 1st, 2022. See the published version at <https://doi.org/10.1016/j.apsusc.2022.153844>.

1 Theoretical proposal of a revolutionary water-splitting
2 photocatalyst: The monolayer of boron phosphide

3

4 Tatsuo Suzuki (鈴木 達夫)¹

5 Tokyo Metropolitan College of Industrial Technology,

6 8-17-1, Minami-Senju, Arakawa-ku, Tokyo, 116-8523, Japan

¹ Electronic mail: dr.tatsuosuzuki@gmail.com

7 **Abstract**

8 Recently, hydrogen generation by water-splitting photocatalysts is attracting attention as a
9 sustainable and clean energy resource. Photocatalytic hydrogen-generation systems are much
10 simpler, cheaper, and easier to scale up than the coupled systems of electrolysis and solar cells,
11 wind-power generation, etc. However, photocatalytic hydrogen generation is currently
12 inefficient. This paper proposes the monolayer of boron phosphide as a stable highly-efficient
13 water-splitting photocatalyst by high-precision density-functional theory calculations using a
14 HSE06 functional with a solvent effect. The monolayer of boron phosphide has a direct allowed
15 energy gap of about 1.4 eV, and functions as a one-step excitation photocatalyst. It absorbs
16 sunlight with wavelengths below about 890 nm (ultraviolet, visible, and near-infrared light) and
17 produces both hydrogen gas and oxygen gas from water at a suitable pH condition. By
18 calculating the overpotentials of hydrogen and oxygen evolution reactions, its photocatalytic
19 effectiveness was confirmed. The monolayers of boron phosphide will realize green hydrogen
20 revolution.

21 Main

22 Fossil fuels cause global warming and will dry up in the future. Nuclear fuel has a risk of
23 radioactive contamination such as Fukushima or Chernobyl. Recently, hydrogen generation by
24 water-splitting photocatalysts ¹ is attracting attention as a sustainable and clean energy resource
25 to replace fossil fuels and nuclear fuel. Photocatalytic hydrogen-generation systems are much
26 simpler, cheaper, and easier to scale up than the coupled systems of electrolysis and solar cells,
27 wind-power generation, etc. Recently, Nishiyama *et al.* ² reported solar hydrogen production
28 from water on a 100 m²-scale using an aluminum-doped strontium titanate particulate
29 photocatalyst. They demonstrated that safe, large-sale photocatalytic water splitting and gas
30 collection and separation were possible; however, the hydrogen production was inefficient.
31 Finding a stable highly-efficient photocatalyst is an urgent task for humankind to realize green
32 hydrogen revolution.

33
34 In 2012, Sun *et al.* ³ reported the fabrication of large-area freestanding single layers of ZnSe
35 with four-atomic thickness, which have an enhanced water-splitting efficiency and photostability.
36 The ZnSe single layers exhibit a photocurrent density of 2.14 mA cm⁻² at 0.72 V versus
37 Ag/AgCl under 300W Xe lamp irradiation, 195 times higher than that of bulk ZnSe. Similarly,
38 the efficiency of SnS₂ single layers is 72 times higher than bulk SnS₂ ⁴, and SnS monolayers is
39 104 times higher than bulk SnS ⁵. These reports reveal that two-dimensional materials can be
40 highly-efficient water-splitting photocatalysts. The possible reason is as follows. In the case of
41 bulk photocatalysts, light penetrates deep inside the photocatalyst, where it generates electron-
42 hole pairs. The generated electrons and holes must move to the surface of the photocatalysts
43 against the mutual Coulomb attraction in order to react with atoms or ions adsorbed on the
44 surface. Therefore, bulk photocatalysts require mechanisms such as depletion layers or
45 heterojunctions to separate electrons and holes; nevertheless, the electrons and holes still
46 recombine, resulting in energy loss. However, in the case of two-dimensional photocatalysts, the
47 generated electrons and holes can instantly react with atoms or ions adsorbed on the surface with
48 little movement because two-dimensional photocatalysts are surface-only materials. Since Sun's
49 reports, many two-dimensional photocatalysts have been developed, and details are found in
50 review articles. ^{6 7 8}

51 Results

52 **Proposal of the monolayer of boron phosphide.** This paper theoretically proposes the
53 monolayer of boron phosphide (BP) as a stable highly-efficient water-splitting photocatalyst (cf.
54 Fig. 1(a)). As a result of searching for various two-dimensional materials by high-precision
55 density-functional theory (DFT) calculations, the revolutionary property of the BP monolayer
56 was discovered. At present, there are no reports that BP monolayers were synthesized. However,
57 in 2019, on the surface of a cubic zinc-blend BP nanocrystal grown at 1250 °C through a solid
58 state reaction route, graphite-like layers with the lattice spacing of 0.35 nm were observed in
59 high-resolution TEM images.⁹ These layers may become the precursors of BP monolayers. In
60 2020, Hernández *et al.*¹⁰ theoretically proposed that BP monolayers can be exfoliated by
61 incorporating arsenic in the (1 1 1) surface of a cubic zinc-blend BP.

62

63 Below, we investigate the property of the BP monolayer as a photocatalyst by two types of
64 high-precision DFT calculations: a plane-wave (PW) basis calculation using a pseudo-potential
65 and a Gaussian type orbital (GTO) basis calculation using all electrons. The PW basis
66 calculation also include a solvent effect, i.e., a water polarization effect by an implicit solvation
67 model based on the Poisson-Boltzmann equation. All calculations use Heyd-Scuseria-Ernzerhof
68 (HSE06) hybrid density functionals^{11 12} for both structural optimizations and energy bands
69 calculations because the HSE06 functional is one of the most reliable calculation methods, and
70 the error between the calculated energy gaps and the experimental values is less than 10%.¹³

71

72 **Important conditions.** First, we confirm four important conditions that two-dimensional
73 photocatalysts must satisfy for large-scale practical use; (a) stable in water against long exposure
74 to strong sunlight, (b) made from earth-abundant elements, (c) one-step excitation using a single
75 semiconductor because Z-scheme using two connected semiconductors requires double photons
76 of one-step excitation, and PEC water splitting using two electrodes causes energy loss due to the
77 complexity of equipment, and (d) a direct allowed transition semiconductor with an energy gap
78 E_g that is larger than the theoretical limit Δ_{limit} but as small as possible. In order to achieve one-
79 step excitation of (c), band edges (i.e., conduction band minimum E_C and valence band
80 maximum E_V) should straddle water redox potentials $E_{\text{H}^+/\text{H}_2}$ and $E_{\text{O}_2/\text{H}_2\text{O}}$; that is,

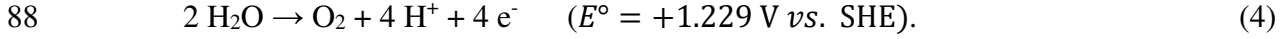
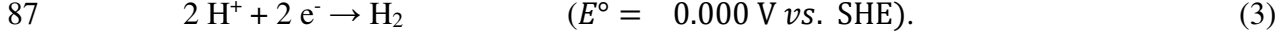
81 $E_C \geq E_{H^+/H_2}$ and $E_{O_2/H_2O} \geq E_V$. (1)

82 And, Δ_{limit} of (d) is the redox potential difference; that is,

83 $E_g = E_C - E_V \geq \Delta_{\text{limit}} = E_{H^+/H_2} - E_{O_2/H_2O}$. (2)

84

85 Next, we confirm redox potentials E_{H^+/H_2} and E_{O_2/H_2O} . The hydrogen evolution reaction
86 (HER) and the oxygen evolution reaction (OER) are expressed in Eqs. (3) and (4), respectively.



89 Water molecules H_2O and hydrogen ions H^+ adsorbed on the surface of the BP monolayer are
90 transformed into various intermediates on the surface (cf. Fig. 1(b)-(h)), and are finally
91 decomposed into hydrogen molecules H_2 and oxygen molecules O_2 , as described in detail below.
92 Here, E° is the standard electrode potential relative to the standard hydrogen electrode (SHE).
93 E_{H^+/H_2} and E_{O_2/H_2O} are expressed by the Nernst equation in Eqs. (5) and (6), respectively.

94 $E_{H^+/H_2} = -4.44 - \frac{RT}{2F} \ln\left(\frac{[H^+]^2}{p_{H_2}}\right) = -4.445 + 0.0592 \text{ pH}$ (eV). (5)

95 $E_{O_2/H_2O} = -4.44 - 1.229 - \frac{RT}{4F} \ln(p_{O_2} \cdot [H^+]^4) = -5.662 + 0.0592 \text{ pH}$ (eV). (6)

96 From the definition of the Nernst equation, E_{H^+/H_2} and E_{O_2/H_2O} are the potential energies of the
97 electron in the BP monolayer, not the potential energies in the solution. The origin of these
98 equations is the vacuum level, and -4.44 eV is the energy level of SHE relative to the vacuum
99 level. F , R , and $[H^+]$ are Faraday constant, gas constant, and the molar concentration of H^+ ions,
100 respectively. Temperature $T = 298.15 \text{ K}$, and $\text{pH} = -\log_{10}[H^+]$. The reaction vessel is filled
101 with generated gas; therefore, the partial pressures of H_2 and O_2 are $p_{H_2} = \frac{2}{3} \text{ atm}$ and $p_{O_2} =$
102 $\frac{1}{3} \text{ atm}$, respectively. The theoretical limit $\Delta_{\text{limit}} = E_{H^+/H_2} - E_{O_2/H_2O} = 1.217 \text{ eV}$.

103

104 **Reviews of previous researches.** First, we review the bulk crystal of BP, which has a cubic
105 zinc-blend structure. The cubic zinc-blend BP is quite chemically stable and is resistant to
106 chemical corrosion. It is not attacked by hot concentrated mineral acids or aqueous alkali
107 solution.¹⁴ It is also resistant to oxidation in air up to about 800-1000 °C.¹⁵ The cubic zinc-

108 blend BP is an indirect transition semiconductor with an energy gap of 2.0 eV, and functions as a
109 photocatalyst for H₂ evolution.^{9 14 16} The photocatalytic H₂ evolution reactions continue even in
110 strong acid or strong alkaline, and the BP photocatalyst is stable under these extreme
111 conditions.¹⁴ These durable properties of the cubic zinc-blend BP originate in the strong
112 covalent bonds between elements B and P. This durability will be carried over to BP monolayers.
113 Recently, Li *et al.*¹⁷ prepared cubic zinc-blend BP nanosheets with a thickness of about 4 nm,
114 and demonstrated that the BP nanosheets were well dispersed in water with a concentration of
115 0.2 mg/mL. Liang *et al.*¹⁸ synthesized cubic zinc-blend BP single crystals larger than 1mm, and
116 evaluated their excellent thermal stability up to 1200 °C.

117
118 Next, we review BP monolayers. The most stable structure of a BP monolayer is a hexagonal
119 planar structure like a graphene or a h-BN monolayer (cf. Fig. 1(a)).¹⁹ Şahin *et al.*²⁰ performed
120 DFT calculations using a PW basis and local-density approximation, and reported the bond
121 length $d = 1.83 \text{ \AA}$ and the direct energy gap $E_g = 0.82 \text{ eV}$ or 1.81 eV which is corrected by
122 frequency-dependent GW_0 calculations. They calculated the phonon dispersion of a BP
123 monolayer also, and confirmed the dynamical stability of a BP monolayer. Suzuki & Yokomizo
124²¹ calculated $d = 1.87 \text{ \AA}$ and $E_g = 1.912 \text{ eV}$ using a GTO basis and a B3LYP/6-31G(d) functional.
125 After that, the high-precision calculation method using a HSE06 functional became widespread.
126 Zhuang & Hennig²² calculated $d = 1.855 \text{ \AA}$ and $E_g = 1.36 \text{ eV}$ using a PW basis and a HSE06
127 functional. Wang & Wu²³ calculated the band edges of a BP monolayer in a vacuum using a
128 PW basis and a HSE06 functional: $d = 1.855 \text{ \AA}$, $E_C = -3.96 \text{ eV}$, and $E_V = -5.33 \text{ eV}$; and
129 showed that the optical absorption of a BP monolayer was strong over a wide energy range
130 between 1.37 and 4 eV. They performed a BOMD simulation by using the Nosé-Hoover method
131 at 2500K for 5 ps, and indicated the high thermal stability of BP monolayers. Furthermore, they
132 reported the chemical stability of BP monolayers in environment, such as N₂, O₂, H₂O, H₂, and
133 CO₂. However, they did not mention the photocatalytic application of BP monolayers. Shu *et*
134 *al.*²⁴ stated that BP monolayers were suitable for a water-splitting photocatalyst based on their
135 calculations using a PW basis, a PBE functional, and the extrapolation of G_0W_0 method.
136 However, their low-precision calculation overestimated the energy gap as $E_g = 1.833 \text{ eV}$.
137 Therefore, the inherent high-efficiency of BP monolayers was not reported correctly, and the
138 photocatalytic effectiveness of BP monolayers has been buried. There are no other papers

139 reporting photocatalytic applications of BP monolayers, except for van der Waals
 140 heterostructures with other monolayers. Wu *et al.*²⁵ performed DFT calculations combined with
 141 *ab initio* molecular dynamics (AIMD) simulations, and demonstrated that the physical and
 142 chemical stabilities of BP monolayers in a vacuum, and in oxygen, water, and oxygen-water
 143 environment.

144

145 **Shapes, potentials, and charge densities.** This paper shows three types of calculated results:
 146 (a) **PWsol** using a PW basis with a solvent effect, (b) **PWvac** using a PW basis in a vacuum, and
 147 (c) **GTOvac** using a GTO basis in a vacuum.

148

149 First, we consider the shapes of BP monolayers after structural optimizations. The bond lengths
 150 of PWsol, PWvac, and GTOvac are 1.845, 1.846, and 1.854 Å, respectively. Comparing PWsol
 151 and PWvac, the bond lengths are almost the same with and without a solvent effect. Comparing
 152 PWvac and GTOvac, there is 0.4% difference in bond lengths due to the different calculation
 153 methods. These bond lengths are in good agreement with previous researches.^{22 23}

154

155 Next, we consider the results of PWsol in Fig. 2. An infinitely wide BP monolayer is placed on
 156 the x-y plane at z=0. $V(z)$ is the potential which is averaged within the unit cell.

$$157 \quad V(z) = \iint_{\text{unit cell}} V_{\text{sol}}(x, y, z) dx dy / \iint_{\text{unit cell}} dx dy, \quad (7)$$

158 where $V_{\text{sol}}(x, y, z)$ is the entire local potential (ionic plus Hartree plus exchange correlation) with
 159 the solvent effect. The potential value at the midpoint of the spacer is vacuum level, and it is
 160 aligned with the origin of energy; that is, $V(z = 9) = 0$. $n(z)$ is the averaged number density of
 161 valence electrons of the BP monolayer with the solvent effect, and $n_b(z)$ is the averaged bound
 162 charge density of water. Drawn for comparison, $V_{\text{vac}}(z)$ is the averaged potential of PWvac, i.e.,
 163 the averaged potential without the solvent effect. $V_{\text{vac}}(z)$ at the midpoint of the spacer is also
 164 aligned with the origin of energy; that is, $V_{\text{vac}}(z = 9) = 0$. We define $V_d(z) \equiv V(z) - V_{\text{vac}}(z)$,
 165 which is the potential difference caused by the polarization of water. Here, we notice that $V_d(z)$
 166 is the vacuum level when the solvent effect exists; that is, $V_d(z)$ corresponds to the vacuum level
 167 of Anderson model²⁶ which explains the energy band profiles of semiconductor heterostructures.
 168 Therefore, $V_H \equiv V_d(z = 0) = 0.21$ eV is the electrical double layer voltage. $E_C = -3.85$ eV
 169 and $E_V = -5.17$ eV are band edges with the solvent effect. $E_{\text{H}^+/\text{H}_2} = -3.90$ eV and $E_{\text{O}_2/\text{H}_2\text{O}} =$

170 -5.12 eV are the redox potentials in Eqs. (5) and (6) at $pH = 9.2$. Here, E_{H^+/H_2} and E_{O_2/H_2O}
171 are based on the vacuum level $V_d(z > 3)$ outside the electric double layer. Under the condition
172 in this figure, the band edges straddle the redox potentials, and Eqs. (1) and (2) are satisfied.

173
174 **Energy bands and redox potentials.** First, we consider energy bands in the left panel of Fig. 3.
175 Here, the energy bands of PWsol and PWvac are drawn under the same condition that $V(z =$
176 $9) = V_{vac}(z = 9) = 0$, as in Fig. 2. The energy bands of GTOvac are also drawn so that the
177 vacuum level is the origin of energy. First, we compare PWsol and PWvac. The energy gaps of
178 PWsol and PWvac are 1.32 and 1.34 eV, respectively. We understand that the difference of
179 energy gaps between with and without the solvent effect is small. The energy gap of PWvac is
180 in good agreement with previous researches.^{22 23} The band edges (E_C, E_V) of PWsol and
181 PWvac are (-3.85, -5.17) and (-4.06, -5.39) eV, respectively. (E_C, E_V) are shifted only by the
182 electrical double layer voltage $V_H = 0.21$ eV. Next, we compare PWvac and GTOvac. The
183 energy gap of GTOvac is 1.47 eV, which is 10% larger than PWvac. This discrepancy is due
184 only to the different calculation methods. (E_C, E_V) of GTOvac is (-4.13, -5.60) eV. Despite the
185 different calculation methods, the band edges (E_C, E_V) are located at almost the same energy
186 levels, which are in good agreement with a previous research.²³

187
188 Next, we consider the relationship between band edges and redox potentials. The band edges in
189 this paper are calculated under the condition that the BP monolayer is not charged, i.e., the pH of
190 the solution is at *the point of zero charge* pH_{pzc} . It is unclear how the band edges of the BP
191 monolayer depend on pH; that is, whether the band edges show a Nernstian dependence of 0.059
192 eV/pH like semiconducting metal oxides (e.g. TiO_2),²⁷ or are pH-independent like a hydrogen-
193 terminated diamond.²⁸ Therefore, we cannot estimate pH_{pzc} . In the right panel of Fig. 3, the
194 redox potentials are drawn according to Eqs. (5) and (6). If the pH_{pzc} of PWsol is in the range of
195 8.4 - 10.0, the BP monolayer functions as a photocatalyst because it satisfies Eq. (1). However,
196 even if the pH_{pzc} is out of this range, the BP monolayer still functions as a photocatalyst. This is
197 because the band edges E_C and E_V are very close to the redox potentials E_{H^+/H_2} and E_{O_2/H_2O} ,
198 respectively; then, either band edge is pinned to the corresponding redox potential.²⁸ By the
199 way, on the BP monolayer side of water-solid interface there is little charge to compensate for

ions adsorbed on the water side because the BP monolayer does not have free electrons like metals nor does it form a depletion layer like bulk semiconductors. Furthermore, the covalent bonds between elements B and P are so strong that B or P does not dissolve as ions. Therefore, the BP monolayer will not be charged very much.

Overpotentials. We calculate the overpotentials of HER and OER by Nørskov approach^{29,30} (see the supplementary information for computational details). Here, we consider an acidic reaction involving H⁺; however, the results are the same for the alkaline reaction involving OH⁻.³² HER pathways considered are (a) H⁺ + e⁻ + * → H*, (b) H⁺ + e⁻ + H* → H₂(g) + *, and (c) 2 H* → H₂(g) + 2 *. OER pathways are (d) H₂O(l) + * → OH* + H⁺ + e⁻, (e) OH* → O* + H⁺ + e⁻, (f) 2 OH* → H₂O(l) + O* + *, (g) H₂O(l) + O* → OOH* + H⁺ + e⁻, (h) OOH* → O₂(g) + * + H⁺ + e⁻, and (i) 2 OOH* → O₂(g) + 2 O* + 2 H⁺ + 2 e⁻. Here, * denotes an adsorb-site on the BP monolayer. In the following, temperature T = 298.15 K. The Gibbs free energies per molecule of hydrogen gas and oxygen gas are $G_{\text{H}_2(\text{g})} = G_{\text{H}_2(\text{g})}^{\circ} + \frac{RT}{F} \ln p_{\text{H}_2}$ and $G_{\text{O}_2(\text{g})} = G_{\text{O}_2(\text{g})}^{\circ} + \frac{RT}{F} \ln p_{\text{O}_2}$, where G° is the Gibbs free energy at standard conditions. The Gibbs free energies of water is $G_{\text{H}_2\text{O}(\text{l})} = G_{\text{H}_2\text{O}(\text{l})}^{\circ} = G_{\text{H}_2\text{O}(\text{g})}^{\circ} - 0.088 \text{ eV}$.³³ $G_{\text{H}_2(\text{g})}^{\circ} = E_{\text{H}_2(\text{g})}^{\text{DFT}} + E_{\text{H}_2(\text{g})}^{\text{ZPE}} + \Delta H_{\text{H}_2(\text{g})}^{\circ}(0 \rightarrow T) - TS_{\text{H}_2(\text{g})}^{\circ}$, and $G_{\text{H}_2\text{O}(\text{g})}^{\circ} = E_{\text{H}_2\text{O}(\text{g})}^{\text{DFT}} + E_{\text{H}_2\text{O}(\text{g})}^{\text{ZPE}} + \Delta H_{\text{H}_2\text{O}(\text{g})}^{\circ}(0 \rightarrow T) - TS_{\text{H}_2\text{O}(\text{g})}^{\circ}$. Here, $E_{\text{H}_2(\text{g})}^{\text{DFT}}$ and $E_{\text{H}_2\text{O}(\text{g})}^{\text{DFT}}$ are the total energies calculated by DFT. $E_{\text{H}_2(\text{g})}^{\text{ZPE}} = \frac{1}{2} h \nu_{\text{H}_2(\text{g}),1}$ and $E_{\text{H}_2\text{O}(\text{g})}^{\text{ZPE}} = \frac{1}{2} \sum_{i=1}^3 h \nu_{\text{H}_2\text{O}(\text{g}),i}$ are the zero-point energies; where h is Plank's constant, and $\nu_{\text{H}_2(\text{g}),1}$ and $\nu_{\text{H}_2\text{O}(\text{g}),i}$ are the calculated frequencies of the normal mode. The enthalpy changes $\Delta H_{\text{H}_2(\text{g})}^{\circ}(0 \text{ K} \rightarrow T)$, $\Delta H_{\text{H}_2\text{O}(\text{g})}^{\circ}(0 \text{ K} \rightarrow T)$, and the standard entropies $S_{\text{H}_2(\text{g})}^{\circ}$, $S_{\text{H}_2\text{O}(\text{g})}^{\circ}$ are taken from the reference.³³ $G_{\text{O}_2(\text{g})}^{\circ} = 2G_{\text{H}_2\text{O}(\text{l})}^{\circ} - 2G_{\text{H}_2(\text{g})}^{\circ} + 4 \times 1.229 \text{ eV}$ which is E° of OER. The sum of Gibbs free energies of a proton and an electron is $G_{\text{H}^+} + G_{\text{e}^-} = \frac{1}{2} G_{\text{H}_2(\text{g})}^{\circ} - \frac{RT}{F} \ln 10 \cdot \text{pH} + V_e$; where V_e is the potential energy of the electron in the BP monolayer relative to SHE. The Gibbs free energy of O* is calculated by $G_{\text{O}^*} = E_{\text{O}^*}^{\text{DFT}} + E_{\text{O}^*}^{\text{ZPE}} - E_{\text{O}^*}^{\text{DFT}}$; where $E_{\text{O}^*}^{\text{DFT}}$ and $E_{\text{O}^*}^{\text{ZPE}}$ are the total energies by DFT, and $E_{\text{O}^*}^{\text{ZPE}} = \frac{1}{2} \sum_i h \nu_{\text{O}^*,i}$ are the calculated zero-point energies. Similarly, G_{OH^*} , G_{OOH^*} , and G_{H^*} are calculated; however, for G_{H^*} we consider four types: G_{H^*0} , G_{H^*1} , G_{H^*2} , and G_{H^*3} . H*0 is a proton adsorbed on the pure surface of the BP monolayer. H*1, H*2, and H*3 are protons adsorbed on the back surface of O*, OH*, and OOH*, respectively (cf.

229 Fig. 1). The overpotentials of HER and OER are defined as $\eta_{\text{HER}} = V_e - E_{\text{H}^+/\text{H}_2}$ and $\eta_{\text{OER}} =$
 230 $E_{\text{O}_2/\text{H}_2\text{O}} - V_e$, which are pH independent. As a result,
 231 $G_{\text{H}_2(\text{g})}$, $G_{\text{O}_2(\text{g})}$, $G_{\text{H}_2\text{O}(\text{l})}$, G_{O^*} , G_{OH^*} , G_{OOH^*} , G_{H^*0} , G_{H^*1} , G_{H^*2} , G_{H^*3} and $G_{\text{H}^+} + G_{\text{e}^-}$ are -6.827, -9.911,
 232 -14.216, -6.392, -9.902, -15.877, -2.555, -2.702, -3.860, -4.322, and $-3.408 - 0.0592 \text{ pH} + V_e$
 233 eV, respectively. Therefore, $\eta_{\text{HER}} = 0.45$ eV along a pathway (a and b) with a H*2 adsorbed-
 234 proton; and $\eta_{\text{OER}} = 0.10$ eV along a pathway (d, e, g, and i) or (d, f, g, and i). By the way, the
 235 difference between the energy gap and the theoretical limit $E_g - \Delta_{\text{limit}}$ are 0.10, 0.12, and 0.25
 236 eV for PWsol, PWvac, and GTOvac, respectively. Although these values are a little smaller than
 237 $\eta_{\text{HER}} + \eta_{\text{OER}}$, the BP monolayer will function well as a photocatalyst under sunlight. The reason
 238 is as follows. When a photon with an energy larger than the energy gap is absorbed, an electron
 239 with an energy larger than E_C and a hole with an energy smaller than E_V are generated. Before
 240 the electron falls to the bottom of the conduction band, the hole rises to the top of the valence
 241 band, or the electron and the hole recombine or form an exciton, the electron and the hole can
 242 react with atoms or ions adsorbed on the surface of the BP monolayer because the BP monolayer
 243 is a surface-only material. This is a great feature that is different from bulk photocatalysts.

244
 245 **Energy gaps and solar radiation spectrum.** Fig. 4 shows the calculated energy gaps of BP
 246 monolayers and solar radiation spectrum (air mass 1.5 global).³⁴ The BP monolayer has an
 247 energy gap of about 1.4 eV. It absorbs sunlight with wavelengths below about 890 nm
 248 (ultraviolet, visible, and near-infrared light), and uses about 48% of the photon flux from the sun
 249 effectively.

250

251 **Conclusions**

252 This paper theoretically proposes the BP monolayer as a highly-efficient water-splitting
 253 photocatalyst. It is a stable semiconductor with a direct allowed energy gap of about 1.4 eV, and
 254 functions as a one-step excitation photocatalyst. It absorbs sunlight with wavelengths below
 255 about 890 nm (ultraviolet, visible, and near-infrared light) and produces both H₂ and O₂ from
 256 water at a suitable pH condition. By calculating the overpotentials of hydrogen and oxygen
 257 evolution reactions, its photocatalytic effectiveness was confirmed. BP monolayers will realize

258 the hydrogen economy as a sustainable and clean energy resource; therefore, we hope that BP
259 monolayers will be synthesized.

260

261 **Methods**

262 **Calculation methods of energy bands.** PW basis calculations use a plane-wave basis set, the
263 projector augmented wave (PAW) potentials,^{35 36} a HSE06 functional, a $27\times 27\times 1$ Monkhorst-
264 Pack k-point mesh, the super-cell width of 18\AA , the cutoff energy of 800 eV for the PW basis,
265 and VASP 5.4.1 package^{37 38}. The convergence criteria of electronic self-consistent calculations
266 and ionic relaxations are 10^{-6} and 10^{-5} eV, respectively. A solvent effect by the polarization of
267 water is implemented as an implicit solvation model based on the Poisson-Boltzmann equation,
268 and is performed by using VASPsol package.^{39 40} GTO basis calculations use a Gaussian type
269 orbital 6-311G(d,p) basis set and a HSE06 functional under the periodic boundary condition. A
270 pseudo-potential is not used because of all-electron calculations. About 2000 k-points are
271 requested in a unit cell. The convergences of electronic self-consistent calculations are that the
272 maximum and the root mean square (RMS) of the variations of the density matrix are less than
273 10^{-5} and 10^{-7} , respectively, and that the variation of the total-energy is less than 10^{-5} Hartree. The
274 convergences of ionic relaxations are that the maximum and RMS of force are less than 2×10^{-6}
275 and 10^{-6} Hartree/Bohr, respectively, and that the maximum and RMS of displacement are less
276 than 6×10^{-6} and 4×10^{-6} Bohr, respectively. The GTO basis calculation is performed by using
277 Gaussian 09 package.⁴¹

278

279 **Calculation methods of overpotentials.** Spin-polarized calculations were performed by using
280 VASP 5.4.4 package, PAW potentials, a PBE functional⁴², a DFT-D3 method for vdW
281 interactions⁴³, and the cutoff energy of 520 eV for the PW basis. The convergence criteria of
282 self-consistent calculations and ionic relaxations were 10^{-5} and 10^{-4} eV, respectively. The
283 adsorbed atoms were calculated with a $2\times 2\times 1$ supercell, a $7\times 7\times 1$ Monkhorst-Pack k-point mesh,
284 and the super-cell width of 18\AA . $\text{H}_2(\text{g})$ and $\text{H}_2\text{O}(\text{g})$ were calculated in a box of $20\text{\AA}\times 20\text{\AA}\times 20\text{\AA}$
285 at Γ k-point.

286

287 **References**

- 288 1. Fujishima, A. & Honda, K. Electrochemical Photolysis of Water at a Semiconductor
289 Electrode. *Nature* **238**, 37–38 (1972).
- 290 2. Nishiyama, H. *et al.* Photocatalytic solar hydrogen production from water on a 100-m²
291 scale. *Nature* **598**, 304–307 (2021).
- 292 3. Sun, Y. *et al.* Fabrication of flexible and freestanding zinc chalcogenide single layers. *Nat.*
293 *Commun.* **3**, 1057 (2012).
- 294 4. Sun, Y. *et al.* Freestanding Tin Disulfide Single-Layers Realizing Efficient Visible-Light
295 Water Splitting. *Angew. Chemie Int. Ed.* **51**, 8727–8731 (2012).
- 296 5. Sun, Y. *et al.* All-Surface-Atomic-Metal Chalcogenide Sheets for High-Efficiency
297 Visible-Light Photoelectrochemical Water Splitting. *Adv. Energy Mater.* **4**, 1300611
298 (2014).
- 299 6. Li, Y., Gao, C., Long, R. & Xiong, Y. Photocatalyst design based on two-dimensional
300 materials. *Mater. Today Chem.* **11**, 197–216 (2019).
- 301 7. Zhao, Y. *et al.* Two-dimensional photocatalyst design: A critical review of recent
302 experimental and computational advances. *Mater. Today* **34**, 78–91 (2020).
- 303 8. Khan, K. *et al.* Recent Progress, Challenges, and Prospects in Two-Dimensional Photo-
304 Catalyst Materials and Environmental Remediation. *Nano-Micro Lett.* **12**, 167 (2020).
- 305 9. Sugimoto, H. *et al.* Size-Dependent Photocatalytic Activity of Cubic Boron Phosphide
306 Nanocrystals in the Quantum Confinement Regime. *J. Phys. Chem. C* **123**, 23226–23235
307 (2019).
- 308 10. Munive Hernández, O. *et al.* Hexagonal boron phosphide monolayer exfoliation induced
309 by arsenic incorporation in the BP (1 1 1) surface: A DFT study. *Appl. Surf. Sci.* **538**,
310 148163 (2021).
- 311 11. Heyd, J., Scuseria, G. E. & Ernzerhof, M. Hybrid functionals based on a screened
312 Coulomb potential. *J. Chem. Phys.* **118**, 8207 (2003).
- 313 12. Heyd, J., Scuseria, G. E. & Ernzerhof, M. Erratum: “Hybrid functionals based on a

- 314 screened Coulomb potential” [J. Chem. Phys. 118, 8207 (2003)]. *J. Chem. Phys.* **124**,
315 219906 (2006).
- 316 13. Park, S., Lee, B., Jeon, S. H. & Han, S. Hybrid functional study on structural and
317 electronic properties of oxides. *Curr. Appl. Phys.* **11**, S337–S340 (2011).
- 318 14. Shi, L. *et al.* n -type boron phosphide as a highly stable, metal-free, visible-light-active
319 photocatalyst for hydrogen evolution. *Nano Energy* **28**, 158–163 (2016).
- 320 15. Williams, F. V. & Ruehrwein, R. A. The Preparation and Properties of Boron Phosphides
321 and Arsenides 1. *J. Am. Chem. Soc.* **82**, 1330–1332 (1960).
- 322 16. Lee, J., Fujishima, A., Honda, K. & Kumashiro, Y. Photoelectrochemical Behavior of p-
323 Type Boron Phosphide Photoelectrode in Acidic Solution. *Bull. Chem. Soc. Jpn.* **58**,
324 2634–2637 (1985).
- 325 17. Li, Z., Cheng, C., Gong, H., Liu, Q. & Huang, C. Water-dispersible boron phosphide
326 nanosheets for enhancing the thermal conductivity of nanofluids. *J. Mol. Liq.* **309**, 113023
327 (2020).
- 328 18. Liang, W. *et al.* Growth of millimeter-size single-crystal boron phosphide by eutectic melt
329 at 5.0 GPa and 3000 °C. *Solid State Commun.* **327**, 114206 (2021).
- 330 19. Suzuki, T. Theoretical discovery of stable structures of group III-V monolayers: The
331 materials for semiconductor devices. *Appl. Phys. Lett.* **107**, 213105 (2015).
- 332 20. Şahin, H. *et al.* Monolayer honeycomb structures of group-IV elements and III-V binary
333 compounds: First-principles calculations. *Phys. Rev. B* **80**, 155453 (2009).
- 334 21. Suzuki, T. & Yokomizo, Y. Energy bands of atomic monolayers of various materials:
335 Possibility of energy gap engineering. *Phys. E Low-dimensional Syst. Nanostructures* **42**,
336 2820–2825 (2010).
- 337 22. Zhuang, H. L. & Hennig, R. G. Electronic structures of single-layer boron pnictides. *Appl.*
338 *Phys. Lett.* **101**, 153109 (2012).
- 339 23. Wang, S. F. & Wu, X. J. First-Principles Study on Electronic and Optical Properties of
340 Graphene-Like Boron Phosphide Sheets. *Chinese J. Chem. Phys.* **28**, 588–594 (2015).
- 341 24. Shu, H., Guo, J. & Niu, X. Electronic, photocatalytic, and optical properties of two-

- 342 dimensional boron pnictides. *J. Mater. Sci.* **54**, 2278–2288 (2019).
- 343 25. Wu, J., Li, J.-H. & Yu, Y.-X. Stabilities of group-III phosphide (MP, M = B, Al, Ga and
344 In) monolayers in oxygen and water environments. *Phys. Chem. Chem. Phys.* **22**, 7633–
345 7642 (2020).
- 346 26. Anderson, R. L. Experiments on Ge-GaAs heterojunctions. *IRE Trans. Electron Devices*
347 **9**, 509–509 (1962).
- 348 27. Xu, Y. & Schoonen, M. A. A. The absolute energy positions of conduction and valence
349 bands of selected semiconducting minerals. *Am. Mineral.* **85**, 543–556 (2000).
- 350 28. Chakrapani, V. *et al.* Charge Transfer Equilibria Between Diamond and an Aqueous
351 Oxygen Electrochemical Redox Couple. *Science* **318**, 1424–1430 (2007).
- 352 29. Nørskov, J. K. *et al.* Origin of the Overpotential for Oxygen Reduction at a Fuel-Cell
353 Cathode. *J. Phys. Chem. B* **108**, 17886–17892 (2004).
- 354 30. Man, I. C. *et al.* Universality in Oxygen Evolution Electrocatalysis on Oxide Surfaces.
355 *ChemCatChem* **3**, 1159–1165 (2011).
- 356 31. Zhu, Y.-A., Chen, D., Zhou, X.-G. & Yuan, W.-K. DFT studies of dry reforming of
357 methane on Ni catalyst. *Catal. Today* **148**, 260–267 (2009).
- 358 32. Liang, Q., Brocks, G. & Bieberle-Hütter, A. Oxygen evolution reaction (OER) mechanism
359 under alkaline and acidic conditions. *J. Phys. Energy* **3**, 026001 (2021).
- 360 33. Lide, D. R. *CRC Handbook of Chemistry and Physics*. CRC Press (2004).
- 361 34. National Renewable Energy Laboratory, Reference Air Mass 1.5 Spectra,
362 <https://www.nrel.gov/grid/solar-resource/spectra-am1.5.html>.
- 363 35. Blöchl, P. E. Projector augmented-wave method. *Phys. Rev. B* **50**, 17953–17979 (1994).
- 364 36. Kresse, G. & Joubert, D. From ultrasoft pseudopotentials to the projector augmented-wave
365 method. *Phys. Rev. B* **59**, 1758–1775 (1999).
- 366 37. Kresse, G. & Hafner, J. Ab initio molecular dynamics for liquid metals. *Phys. Rev. B* **47**,
367 558–561 (1993).
- 368 38. Kresse, G. & Furthmüller, J. Efficient iterative schemes for ab initio total-energy
369 calculations using a plane-wave basis set. *Phys. Rev. B* **54**, 11169–11186 (1996).

- 370 39. Mathew, K., Sundararaman, R., Letchworth-Weaver, K., Arias, T. A. & Hennig, R. G.
371 Implicit solvation model for density-functional study of nanocrystal surfaces and reaction
372 pathways. *J. Chem. Phys.* **140**, 084106 (2014).
- 373 40. Mathew, K., Kolluru, V. S. C., Mula, S., Steinmann, S. N. & Hennig, R. G. Implicit self-
374 consistent electrolyte model in plane-wave density-functional theory. *J. Chem. Phys.* **151**,
375 234101 (2019).
- 376 41. Frisch, M. J. *et al.* Gaussian 09, Revision C.01, Gaussian Inc., Wallingford CT (2010).
- 377 42. Perdew, J. P., Burke, K. & Ernzerhof, M. Generalized Gradient Approximation Made
378 Simple. *Phys. Rev. Lett.* **77**, 3865–3868 (1996).
- 379 43. Grimme, S., Antony, J., Ehrlich, S. & Krieg, H. A consistent and accurate ab initio
380 parametrization of density functional dispersion correction (DFT-D) for the 94 elements
381 H-Pu. *J. Chem. Phys.* **132**, 154104 (2010).

382

383 **Acknowledgements**

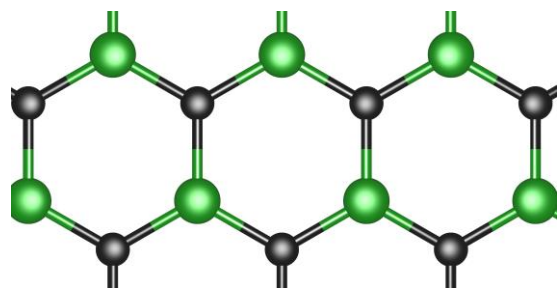
384 This work was partially supported by Tokyo Metropolitan College of Industrial Technology.

385

386 **Competing interests**

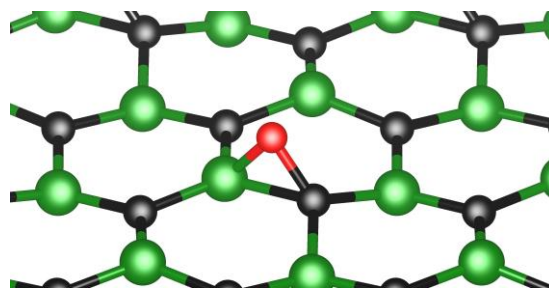
387 The author declares no competing interests.

388



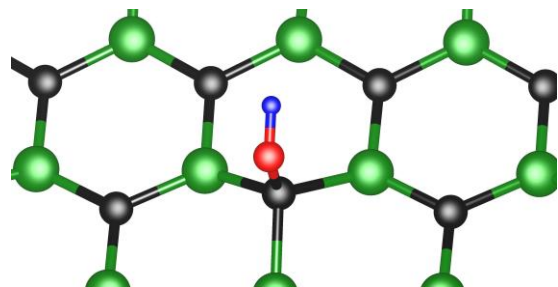
389

(a)



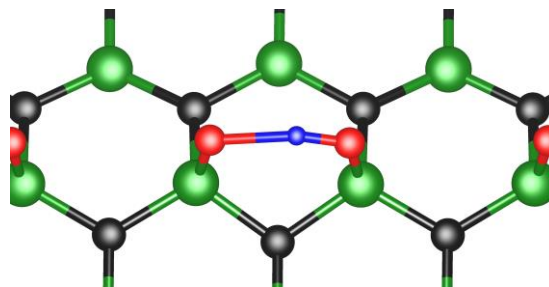
(b)

390



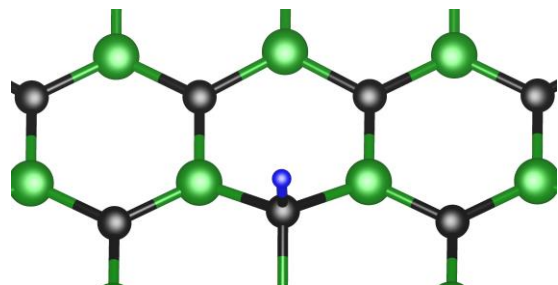
391

(c)



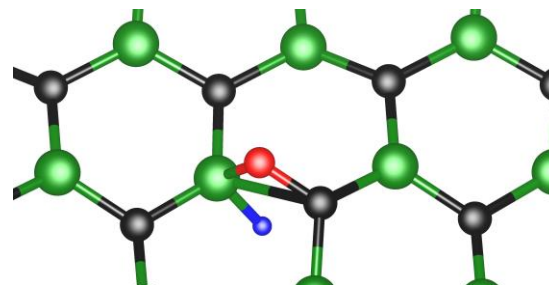
(d)

392



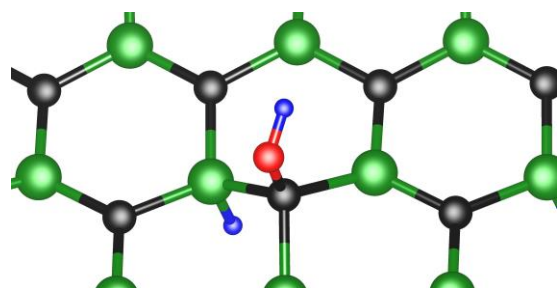
393

(e)



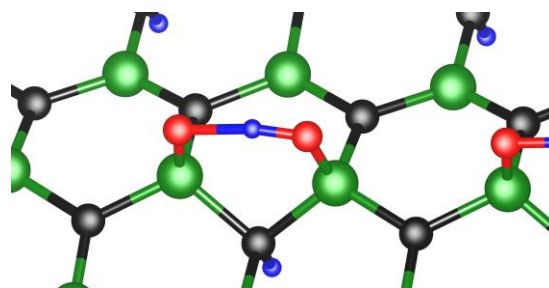
(f)

394



395

(g)



(h)

396

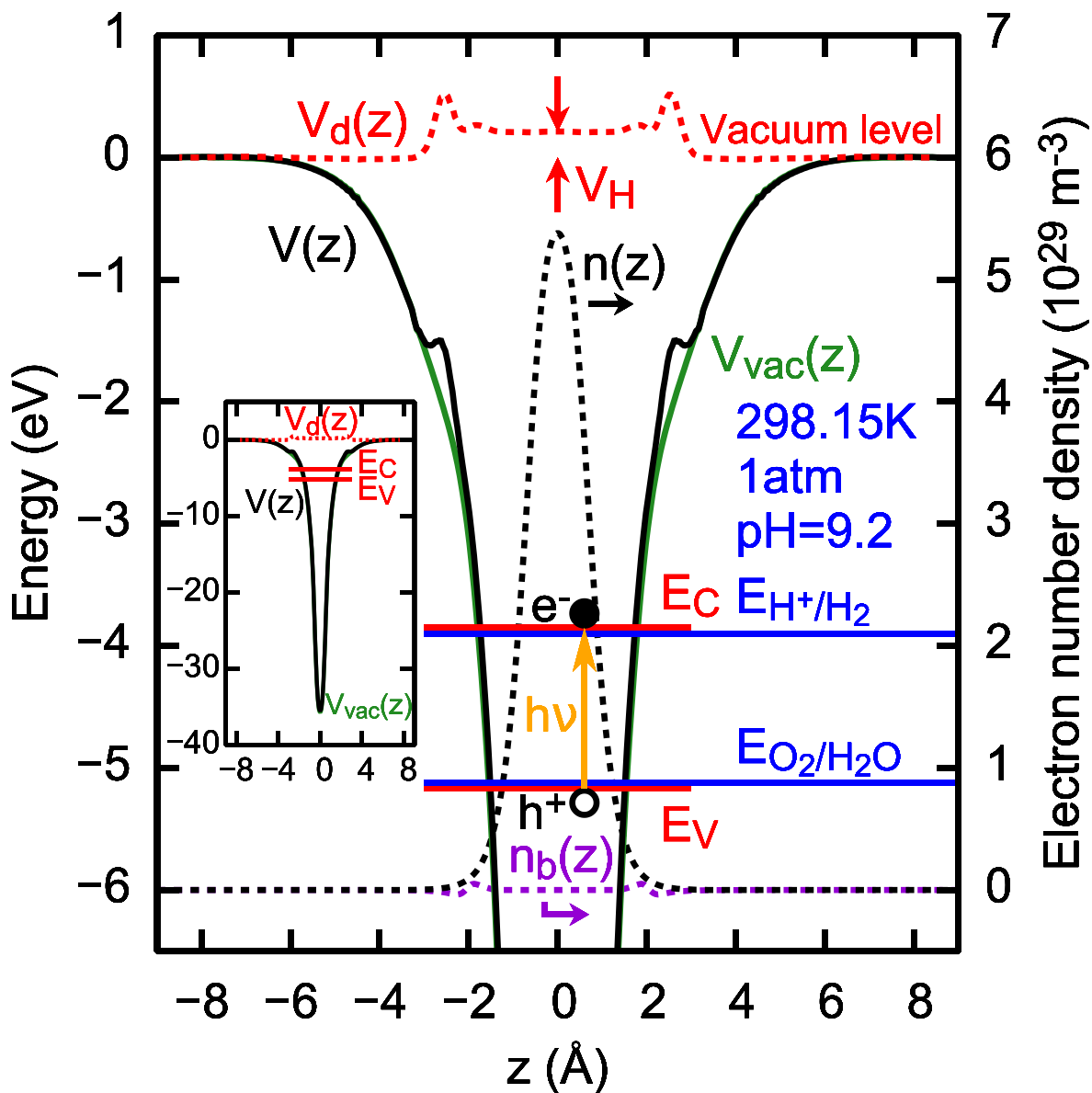
Figure 1. Optimized structures of (a) BP monolayer, (b) O*, (c) OH*, (d) OOH*, (e) H*0,

397

(f) H*1, (g) H*2, and (h) H*3. Black, green, red, and blue balls are boron, phosphorus,

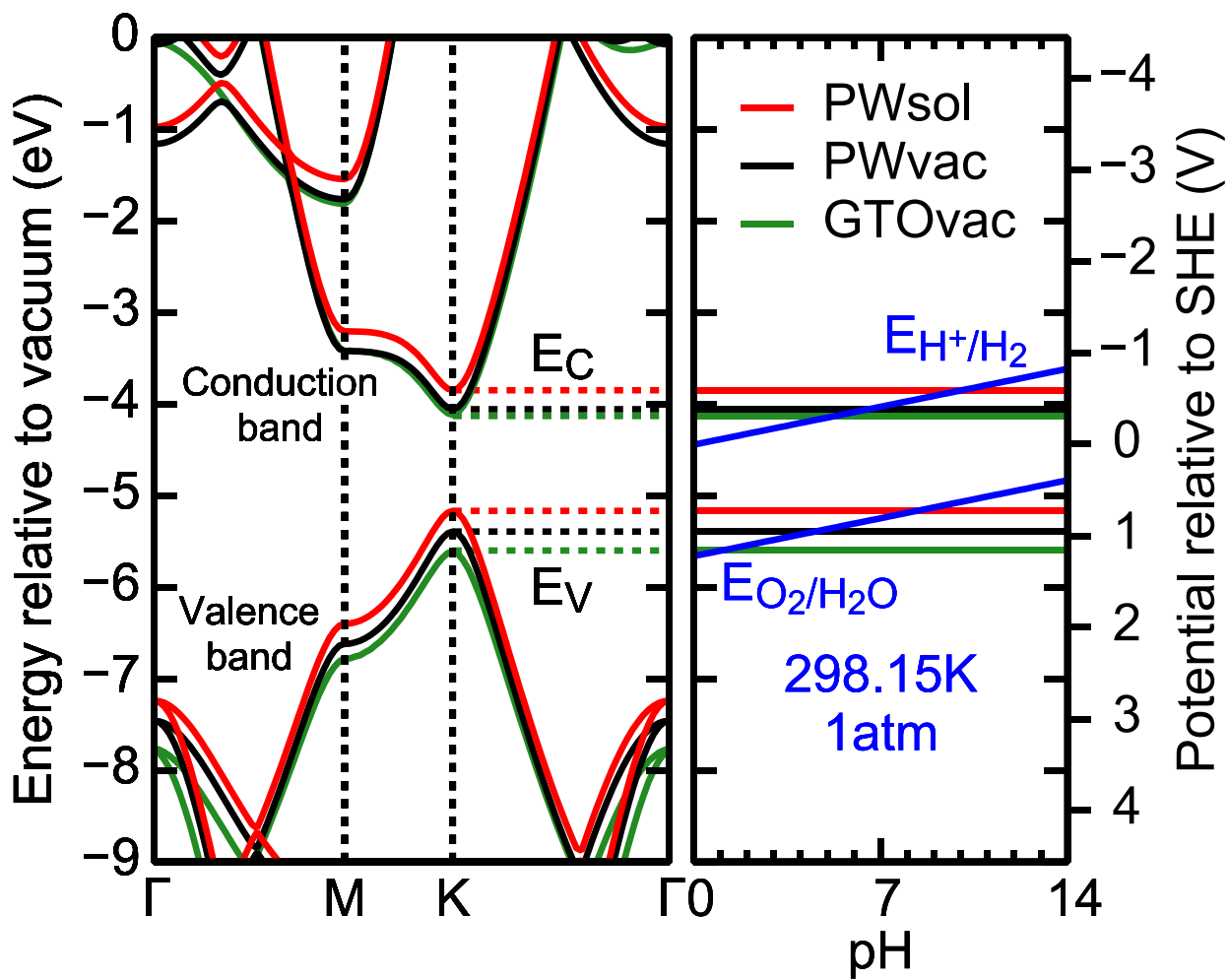
398

oxygen, and hydrogen atoms, respectively.



399

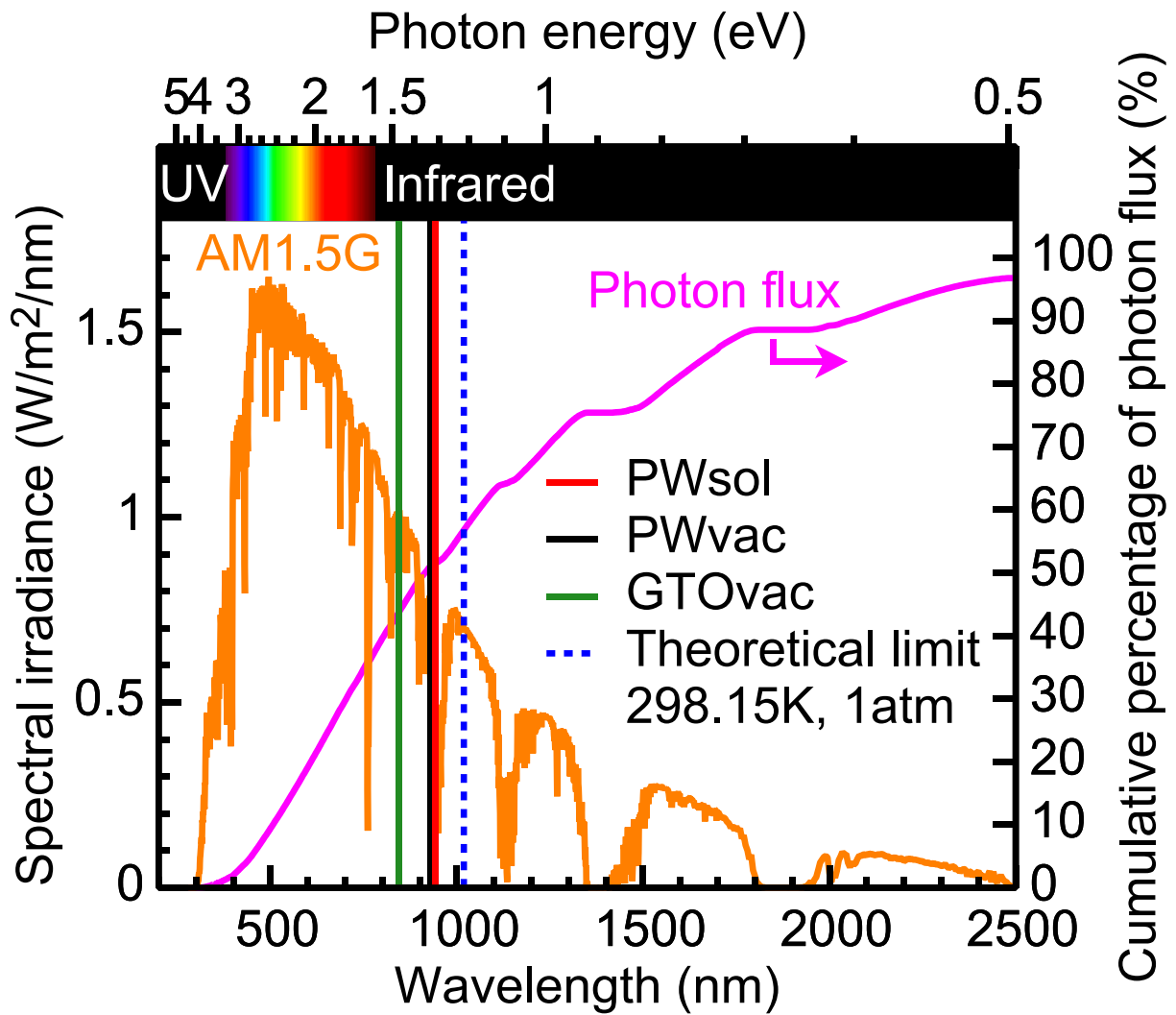
400 **Figure 2.** Potentials, charge densities, and band edges vs. a z-coordinate. The inset is an
 401 overall view.



402

403

Figure 3. (Left panel) energy bands. (Right panel) band edges and redox potentials vs. pH.



404

405 **Figure 4.** Calculated energy gaps, solar radiation spectrum (air mass 1.5 global), and photon
 406 flux vs. wavelength.

Supplementary Files

This is a list of supplementary files associated with this preprint. Click to download.

- [TatsuoSuzukiNatureCatalysisSupplementaryInformationI20220329.pdf](#)